Journal of Basrah Researches (Sciences) **51**(2), 116 (2025)
DOI: https://doi.org/10.56714/bjrs.51.2.9

Hybrid Image Inpainting Using Wavelet and Cahn-Hilliard Model

Nada S. AL-Fartosi*, Ahmed K. Al-Jaberi

Mathematics Department, College of Education for Pure Science, the University of Basrah, Iraq.

ARTICLE INFO

Received 27 September 2025
Revised 25 October 2025
Accepted 30 October 2025
Published 31 December 2025

Keywords:

Image Inpainting, Frequency Domain, Discrete Wavelet Transform (DWT), Cahn-Hilliard Equation, Implicit Finite Differences Method.

Citation: N. S. AL-Fartosi, A. K. Al-Jaberi, J. Basrah Res. (Sci.) **50**(2), 116 (2025). DOI:https://doi.org/10.56714/bjrs.51.2.9

ABSTRACT

With a wide range of applications in digital image processing, including multimedia editing, medical imaging, and cultural heritage preservation, image restoration is a fundamental task. In this work, we present a hybrid image restoration framework that combines a diffusion model based on the Cahn-Hilliard equation with a single-level wavelet transform to decompose an image into distinct frequency components. To maintain structural continuity, this hybrid method leverages the benefits of wavelets in the frequency domain for texture reconstruction and their propagation capabilities in the spatial domain. To achieve smooth information propagation and maintain edge sharpness, the finite implicit finite difference approach is used to solve the problem numerically. The effect of several types of wavelets was analyzed, including Haar, db1, sym1, bior1.1, db4, sym4, coif3, and others. The results indicate that the performance of wavelets varies depending on the length of the support and the smoothness of the fundamental functions, and provide practical guidance for selecting the most suitable wavelet for image restoration in modern image processing applications.

1. Introduction

The image serves as a vehicle for expression and communication, supplanting several other forms of communication. Nevertheless, the image may be incomplete due to various factors, including inadequate storage and adverse weather conditions. Image inpainting is a technique designed to restore damaged regions of an image, thereby reconstructing it and delivering a high-quality semantic representation of the original image [1][2]. Yi Huang and colleagues introduced a Wavelet-Based Diffusion Model (WaveDM). WaveDM ensures the distribution of pristine images in the wavelet domain, dependent on the wavelet spectrum of degraded images post-wavelet transformation; hence, it improves time efficiency in each sampling phase compared to spatial domain modelling. A distinctive training methodology is employed to enhance restoration efficacy, utilizing independent modules to acquire low-frequency and high-frequency spectrums. WaveDM is approximately 100 times faster than current image restoration algorithms that employ standard diffusion models and exhibit performance that is comparable to traditional one-pass techniques [3]. Z. Kareem and A. AL-Jaberi reviewed and examined ways for recovering absent regions in digital photographs within both spatial and frequency domains, emphasizing the constraints of pixel-based

*Corresponding author email: nada.sarhan@uobasrah.edu.iq

ISSN: 1817-2695 (Print); 2411-524X (Online)
Online at: https://jou.jobrs.edu.iq

methods in enhancing all image attributes. Consequently, the researcher utilizes mathematical transformations, namely the discrete wavelet transform (DWT) with Haar wavelets, as a crucial instrument for attaining successful processing outcomes [4]. A. Kiruluta and A. Lemos described an innovative generative modelling framework, Wavelet-Fourier-Diffusion. This framework modifies the diffusion paradigm to incorporate hybrid frequency representations for the production of high-quality, high-fidelity images with enhanced spatial localization. Unlike traditional diffusion models that depend solely on additive noise in pixel space, their method utilizes a multi-transform that integrates wavelet sub-band decomposition with partial Fourier steps. This method systematically deteriorates and subsequently reconstructs images within a hybrid spectral domain during the forward and reverse diffusion phases [5]. Y. Yu et al. introduced a wavelet-based inpainting network that disaggregates images into separate frequency bands and reconstructs the absent segments within each band autonomously and explicitly. WaveFill uses the discrete wavelet transform (DWT) to automatically maintain spatial information during image decomposition. Extensive tests on numerous datasets show that WaveFill achieves better image inpainting in terms of both quantity and quality [6],

R. Chan et al. provided an innovative wavelet-based inpainting algorithm. By incorporating principles of anisotropic regularization and diffusion, models can more effectively rectify damaged pixels at edges. They investigated the algorithms employing forward-backward splitting methods in convex analysis and established that they satisfied the convergence criteria. Numerical examples demonstrate the efficacy of algorithms [7]. Emerging difficulties include the fact that the resulting inpainting regions in the pixel domain are often not geometrically well-defined and that degradation is frequently spatially inhomogeneous. T. Chan et al. proposed two interconnected variational models to address these issues, integrating total variation (TV) minimization techniques with wavelet representations. The Euler-Lagrange equations yield nonlinear partial differential equations (PDEs) in the wavelet domain, necessitating the development of suitable numerical methods and strategies for their solution [8]. A. Averbuch et al. introduced a novel algorithm for the image inpainting problem. The method employs a newly developed, customizable library of quasi-analytic complex-valued wavelet packets (qWPs) derived from polynomial splines of various orders. The tensor products of one-dimensional wave packets generate a variety of two-dimensional wave packets aligned in several directions. The results achieved for this challenge are highly competitive with the leading state-of-the-art algorithms [9].

Sijin He, Guangfeng Lin, Tao Li, and Yajun Chen suggested an image interpolation technique based on frequency-domain transformers. The technique improves multi-scale structure modeling and maintains fine details by introducing an attention mechanism that combines the Wavelet transform and Gabor filtering. Additionally, the conventional forward network is intended to be replaced by a frequency-domain learnable filter based on the Fast Fourier Transform, which allows adaptive noise reduction while maintaining image features. According to experimental data, this technique preserves more high-frequency information, which drastically improves the quality of image interpolation [10]. B. Dong et al. established a fundamental connection between wavelet minimization and nonlinear partial differential equations (PDEs), paving the way for the advancement of novel PDE models and sophisticated image restoration methodologies. This study also illustrates that nonlinear evolution equations, encompassing both parabolic and hyperbolic types, can be approximated by meticulously crafted wavelet and reduction frameworks. This study transcends the constraints of conventional image restoration by presenting wavelet minimization as an innovative method for addressing partial differential equations (PDEs). The results obtained enhance the theoretical framework and broaden the numerical applications of wavelets and partial differential equations (PDEs) [11]. H. Zhang et al. introduced a wavelet decomposition technique for image inpainting. The compromised image is initially segmented into structural and textural sub-images by wavelet processing. The sub-image lacking structural information is reconstructed via the Curvature-Driven Diffusions (CDD) technique.

In contrast, the corresponding region in the texture sub-image is completed by sophisticated exemplar-based texture synthesis. The ultimate image is produced by amalgamating the rectified structural and textural elements. Numerous studies demonstrate that the proposed technique can rapidly and effectively retrieve both structural and textural information concurrently [12]. R. Chan

et al. employed an unconstrained, TV-regularized data-fitting model to reconstruct the image. The alternate direction method (ADM) is utilized to solve the model. The ADM must resolve three subproblems at every iteration, each having a closed-form solution. The predominant per-iteration processing expense of the ADM is ascribed to two Fourier transforms and two wavelet transforms, which collectively enable swift computing. Comparative numerical data between the ADM and other innovative algorithms is also accessible [13]. W. Guo and L. Qiao examine the difficulties associated with recovering deficient or absent coefficients in both spatial and wavelet domains. They initially suggest a method for the automated restoration of elongated and narrow voids in the spatial domain. By adjusting the algorithm's weights based on the image's characteristics, they can improve inpainting results while markedly decreasing computing time. Secondly, they provide an alternative novel method for tackling inpainting difficulties using wavelets. Despite losing as much as 90% of the wavelet coefficients, the process remains straightforward and exhibits considerable recovery effectiveness [14]. Nevertheless, most previous research has been limited to either diffusion models within the spatial domain or wavelet representations in isolation, without an effective integration of the two approaches. Furthermore, the impact of various wavelet families on the restoration process has been inadequately investigated. Yu Cao, Ran Ma, Kaifan Zhao, and Ping An presented an advanced image filling algorithm called WFIL-NET, which combines wavelet downloading and a frequency-integrated learning module. The model is based on a Generative Adversarial Network (GAN) architecture with an encoder-decoder generator to improve feature representation. The wavelet module extracts structural information and texture details from different frequency bands, while the attention mechanism efficiently fuses this information. This fusion makes sure that the restored images have both structural and semantic consistency. Experimental results on the Places2 and CelebA-HQ databases demonstrate high visual quality and reduced artifacts when processing large and irregular missing regions in images [15]. Kolodochka and Polyakova tackle the issue of picture restoration inside deep learning computer vision frameworks. The research seeks to enhance restoration efficacy by integrating the wavelet transform into the LaMa-Fourier network framework. The researchers suggest substituting the spectral unit derived from the Fourier transform with a three-dimensional wavelet transform utilizing the Daubechies db4 wavelet, processing each subband independently before inverting it. Experimental findings demonstrate that the novel LaMa-Wavelet network surpasses the original network in PSNR metrics by roughly 4.5% for narrow and medium apertures and by approximately 6% for large apertures. The SSIM value rises by 2–4%, accompanied by a threefold increase in execution time. The visual analysis indicates that the enhancements in the network are most evident on intricate backgrounds, including recurring patterns[16] .

This research presents a hybrid model that combines the Cahn-Hilliard diffusion equation with a single-level wavelet transform, systematically evaluating several types of wavelets. This combination aims to achieve a better balance between structural continuity and texture restoration accuracy, therefore delivering enhanced reconstruction quality compared to traditional single-domain methods. The subsequent sections of the paper are organized as follows: Section 2 shows the Cahn-Hilliard model that was proposed for restoring images. Section 3 introduces the concept of the frequency domain. Section 4 analyzes the proposed algorithm, including the processing sequence from the input of corrupted images to their reconstruction and assessment. Section 5 outlines and examines several numerical results of the suggested model. Section 6 will articulate the conclusion and specify future initiatives.

2. Modified Cahn-Hilliard Model

One semi-linear fourth–order partial differential equation (PDE) developed for binary image inpainting is modified Cahn-Hilliard (mch) equation [17]. Field of material sciences use of this equation [18]. with $\overrightarrow{x} = (x, y)$ and let $D \subset \Omega$ representing the inpainting domain, Let $f(\vec{x})$ be a specified image defined throughout the domain Ω. The equation is given by:

$$\partial_t u = \Delta\left(-\epsilon\ \Delta u - \frac{1}{\epsilon} F`(u)\right) + \lambda\,(\vec{x})(f(\vec{x}) - u), \qquad \text{in } \Omega \tag{1}$$

Where: $(\vec{x}) = \begin{cases} 0 & \text{if } \vec{x} \epsilon\ D \\ \lambda_0 & \text{if } \vec{x}\ \epsilon\, \Omega \backslash D \end{cases}$

Equation (1) is known as the mCH equation, which includes an additional fidelity term $\boldsymbol{\lambda}(\vec{x})$ $(f-u)$. The function $F(u)$ is referred to as a double–well potential, given by $\boldsymbol{F(u)=\frac{1}{u}\,(1-u)^2}$, and ϵ is a tiny positive parameter that approaches zero. To solution Equation (1), it is sufficient on minimize following energy functional:

$$\int_{\Omega}\left(\frac{\epsilon}{2}|\nabla u|^2+\frac{1}{\epsilon}f(u)\right)d\vec{x}+\lambda_0\int_{\Omega\setminus D}(f-u)^2\,d\vec{x} \tag{2}$$

The initial component denotes energy of a gradient flow based on H^{-1}-norm, resulting in mCH equation, whereas subsequent component is a fidelity term derived from a gradient flow utilising the L^2-norm. This process is similar to the convexity splitting used in an isotropic framework. Diffusion inpainting functions under a fourth-order total variation framework. The fitting term represents a gradient flow in $H^{-1}(\Omega)$. The fidelity term is considered on $L^2(\Omega)$. In this context, $H^{-1}(\Omega)$ is the dual Sobolev space of $H_0^1(\Omega)$, with associated norm defined as:

$$\|f\|_{-1}^2=\|\nabla\Delta^{-1}f\|_{-1}^2=\int_{\Omega}(\nabla\Delta^{-1}f)^2\,d\vec{x} \tag{3}$$

Where Δ^{-1} refers to inverse of the Laplace operator, such that $u=\Delta^{-1}f$ is $-\Delta u=f$, in Ω, with $u=0$ on $\partial\Omega$ Let:

$$R_1=\int_{\Omega}\left(\frac{\epsilon}{2}\,|\nabla u|^2+\frac{1}{\epsilon}\,F(u)\right)d\vec{x}, \tag{4}$$

$$R_2=\lambda_0\int_{\Omega\setminus D}(f-u)^2\,d\vec{x} \tag{5}$$

A convexity splitting is applied separately to R_1 and R_2 is decomposed as:

where R_1=$R_{11}-R_{12}$, then

$$R_{11}=\int_{\Omega}\left(\frac{\epsilon}{2}\,|\nabla u|^2+\frac{C_1}{2}\,|u|^2\right)d\vec{x}, \tag{6}$$

$$R_{12}=\int_{\Omega}\left(-\frac{1}{\epsilon}\,F(u)+\frac{C_1}{2}\,|u|^2\right)d\vec{x} \tag{7}$$

Like wise R_2=$R_{21}-R_{22}$, where:

$$R_{21}=\int_{\Omega\setminus D}\frac{C_2}{2}\,|u|^2\,d\vec{x}, \tag{8}$$

$$R_{22}=\int_{\Omega\setminus D}(-\lambda_0\,(f-u)^2)+\frac{C_2}{2}\,|u|^2\,d\vec{x} \tag{9}$$

Based on the above, the resulting time-stepping scheme is given by:

$$\frac{u^{n+1}-u^n}{k}+\epsilon\,\nabla^4\,u^{n+1}-C_1\,\nabla^2\,u^{n+1}+C_2\,u^{n+1}$$
$$=\nabla^2\left(\frac{1}{\epsilon}\,f`(u^n)+\lambda(\vec{x})\,(f(\vec{x})-u^n)\right)-C_1\,\nabla^2\,u^n+C_2\,u^n \tag{10}$$

The significance of this model lies in its ability to restore large missing regions without introducing artifacts [17].

3. Frequency domain

The frequency domain is a crucial tool in image processing, enabling the examination of an image's frequency content rather than merely addressing it in the spatial domain. This transformation distinguishes low-frequency components linked to gradual gradients and overall lighting from high-frequency components related to intricate details and edges. Operating in the frequency domain offers enhanced versatility in implementing filtering, data compression, and restoration methodologies. The Fourier transform is a prevalent transformation in this domain, offering a comprehensive representation of frequencies without indicating their specific locations. It is proficient in interpreting periodic images and overarching patterns, although it is deficient in spatial accuracy [19]. The wavelet transform was developed to address this issue, integrating spatial and frequency analysis concurrently at various degrees of precision and enhancing its efficacy in image processing, particularly in restoration and data reduction applications [20]. The discrete cosine transform is extensively utilized in picture compression, such as JPEG, since it effectively contains the majority of energy inside a limited set of frequency coefficients [21]. The two-dimensional discrete wavelet transform (DWT) decomposes the image into several frequency components, which can be examined using different wavelet analysis filters, including the Haar wavelet and Daubechies wavelet. Initially, the Discrete Wavelet Transform (DWT) operates horizontally across the image rows, decomposing it into four sub-bands: a low-frequency sub-band

(LL) and three high-frequency sub-bands (HH, HL, LH). The LL sub-band comprises low frequencies in both horizontal and vertical directions, while the LH, HL, and HH sub-bands contain high frequencies in the vertical, horizontal, and diagonal directions, respectively.

4. Inpainting-Based Cahn-Hilliard Model in The Frequency Domain

To implement the Cahn-Hilliard model, the image must initially undergo a mathematical transformation via the discrete wavelet transform (DWT) to transition from the spatial domain to the frequency domain. The original and damaged images are decomposed into low- and high-frequency components using several wavelet functions (Haar, sym4, bior6.8, etc.). Each image is partitioned into four sub-bands at the initial wavelet level, but the size of the mask image should be the same size as the original image. We follow the work in [22]. The algorithm can represent the inpainting image in the frequency domain as follows:

1. The user manually designates the color image area.
2. Diverse wavelet functions are employed to deconstruct both the original and corrupted images into low- and high-frequency components, resulting in four sub-bands at the initial wavelet level.
3. The Cahn-Hilliard model is utilized to recreate the missing region in each of these sub-bands.
4. The inverse wavelet transform is employed to produce the in-painted image.

Figure 1 illustrates a method for generating the image utilizing the Wavelet Transform (WT) in the frequency domain.

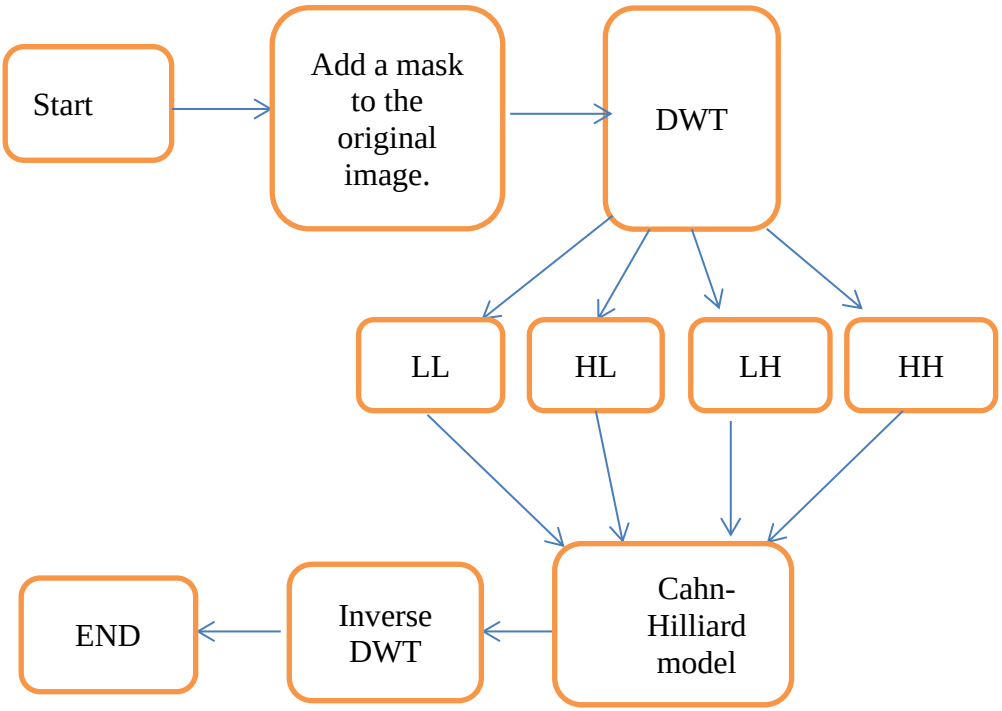

Fig. 1. Flowchart of image inpainting process using a wavelet transform and Cahn-Hilliard model.

5. Numerical experiments and results

Numerical experiments were performed on 80 natural color photos exhibiting both low and high textures retrieved from the Berkeley database. As shown in Figure 2, the work was executed in the RGB color space to attain precise restoration of color details. Regions absent from the photos were incorporated using four distinct masks: mask 1 (a small absent region), mask 2 (a medium

absentregion), mask 3 (a large absent region), and mask 4 (depicting two extensive scratches). As illustrated in Figure 3.

Fig. 2. Example of four out of 80 trained natural images.

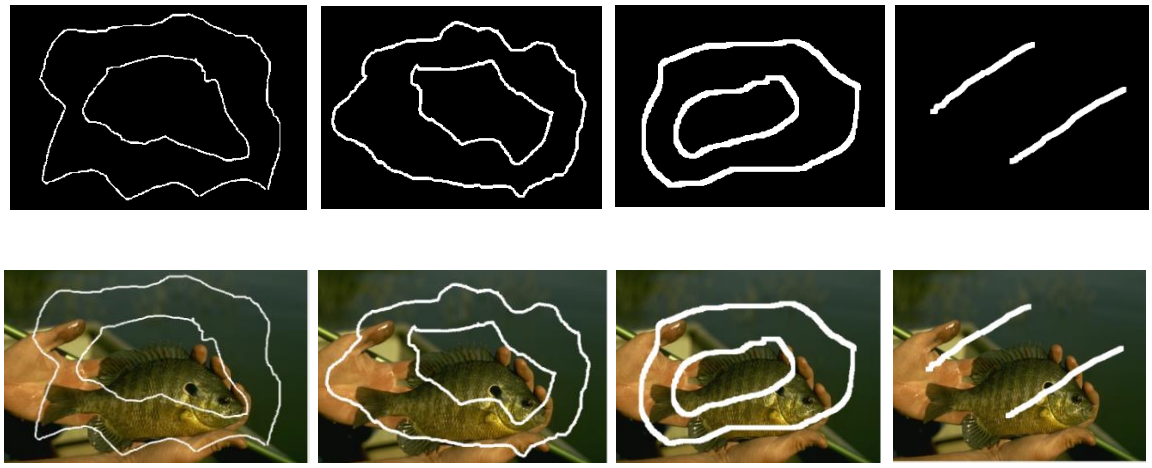

Fig. 3. Types of masks and damaged images; the first row: (binary masked images), and the second row: (color-damaged images).

Two primary experiments were conducted utilizing the suggested algorithm, altering the four previously described masks. To assess the impact of wavelet types on performance, many families of wavelets were examined, including:

1- Haar
2- Symlets (sym1, sym4, sym6)
3- Daubechies (db1, db4, db6)
4- Biorthogonal (bior1.1, bior4.4, bior6.8)
5- Coiflets (coif3)

Thereafter, we use Structural quality measures (SQMs), including structural similarity indices (SSIM) [23], peak signal-to-noise ratio (PSNR) [24], mean square error (MSE) [25]. We also evaluate the information entropy of both the input image E_0 and the output image E_1. To visually and statistically compare the experiment outcomes These SQMs are used to evaluate the model's efficiency in terms of its ability to retrieve missing regions from the image. The time taken to obtain results was also studied, and the image recovery was implemented in MATLAB code (elapsed for MATLAB R2020a, running on a laptop with an Intel (R) Core (TM) i7-9850H CPU at 2.60 GHz and 32 GB of RAM). Two experiments were conducted in this section. Section 5.1 presents an experiment analyzing the model's behavior on missing regions of different sizes; Section 5.2 presents an experiment analyzing the model's behavior on different numbers of iterations.

5.1. Different Types of Missing Areas

To achieve a thorough and accurate assessment, four experiments were carried out to measure the restoration performance using four distinct masks that represented different degrees of image damage. The size of the deleted region in each mask varied. For each wavelet, the optimal iteration (13) was used in all experiments to attain consistent results. Eight wavelet types were used in the investigation, including the Haar, sym1, db1, and bior1.1. Because they produce consistent results across all measurements, they are regarded as a single wavelet [26]. Eight wavelets were obtained by adding the remaining wavelets. Finding the optimal wavelet for picture restoration under various damage levels and examining how wavelet type affects the quality of the output were the objectives of this comparison. The measured values for the different wavelets are displayed in the following tables based on the evaluation criteria and the four masks.

Table 1. The average values of MSE, PSNR, SSIM, and entropy for image inpainting using a hybrid model in MASK 1 at iteration 13.

Wavelets	MSE	PSNR	SSIM	E_0	E_1	Time(s)
Haar	40.15517	36.13894	0.983176	7.146816	5.840143	4.5963
bior4.4	43.57188	37.45256	0.98569	7.146816	7.101395	4.2156
coif3	44.74652	37.13688	0.985217	7.146816	7.098869	4.7426
db4	44.84395	36.95435	0.984812	7.146816	7.103841	4.646
sym4	45.27931	36.90573	0.984495	7.146816	7.104446	5.9405
sym6	45.83697	37.05031	0.984822	7.146816	7.101134	5.7739
db6	46.06309	37.08348	0.984778	7.146816	7.102581	4.5521
bior6.8	46.51745	37.48613	0.985956	7.146816	7.098623	5.7612

It's worth noting that all four experiments were ranked according to MSE values, from lowest to highest, to better illustrate performance. The results in Table 1 above show that the lowest MSE was achieved when using the Haar wavelet, indicating that it reduced the numerical differences between the original and reconstructed images better than other wavelets. The bior6.8 wavelet recorded the highest PSNR and SSIM values. In terms of entropy (E_1), most wavelets produced values close to the original value. Haar, on the other hand, produced a much lower value, reflecting a loss of information compared to the original, while the bior4.4 wavelet performed best in terms of speed.

Table 2. The average values of MSE, PSNR, SSIM, and entropy for image inpainting using a hybrid model in MASK 2 at iteration 13.

Wavelets	MSE	PSNR	SSIM	E_0	E_1	Time(s)
db4	84.72335	31.64431	0.956918	7.146816	7.097304	4.6126
sym4	84.75701	31.72975	0.956283	7.146816	7.094253	5.0963
db6	85.69688	31.72288	0.955588	7.146816	7.099884	4.6615
sym6	85.98829	31.61191	0.953837	7.146816	7.094406	4.6976
bior4.4	87.39934	31.31131	0.953154	7.146816	7.096048	4.4048
coif3	87.97494	31.5791	0.955689	7.146816	7.097774	5.9658
bior6.8	90.13345	31.5921	0.955376	7.146816	7.093413	4.4584
Haar	98.41994	30.82686	0.961481	7.146816	5.840143	4.696

From the results of the first experiment, also on the deleted region mask 2, we obtained the following results:db4 achieved the best numerical performance (lowest MSE), while sym4 provided the highest PSNR value in terms of visual quality. Haar recorded the highest SSIM, and coif3 showed superiority in the resulting entropy due to its proximity to the original. In terms of execution time, bior6.8 was the fastest.

Table 3. The average values of MSE, PSNR, SSIM, and entropy for image inpainting using a hybrid model in MASK 3 at iteration 13.

Wavelets	MSE	PSNR	SSIM	E_0	E_1	Time(s)
db6	829.1771	19.09319	0.856127	7.146816	7.204098	4.5964
sym6	851.2765	18.97345	0.855084	7.146816	7.159188	4.5665
db4	868.4773	18.88954	0.854272	7.146816	7.186705	4.669
sym4	871.6406	18.87203	0.854087	7.146816	7.160376	4.7001
bior4.4	912.2014	18.67299	0.851602	7.146816	7.164469	4.4066
coif3	949.2711	18.50603	0.853067	7.146816	7.198578	5.959
bior6.8	969.2993	18.4142	0.852619	7.146816	7.168238	4.5516
Haar	988.7006	18.3311	0.854798	7.146816	5.840143	4.5152

Here in Table 3, over a large missing region (mask 3), db6 performed best in terms of quality (MSE, PSNR, SSIM), while the Haar wavelet performed the worst. The fastest was the bior4.4 wavelet. In Table 4, the results are as follows: the best in terms of (MSE, PSNR) was the bior4.4 wavelet. The poorest performance was achieved with the Haar wavelet, with db6 recording the highest SSIM, and the fastest was the bior4.4 wavelet.

Table 4. The average values of MSE, PSNR, SSIM, and entropy for image inpainting using a hybrid model in MASK 4 at iteration 13.

Wavelets	MSE	PSNR	SSIM	E_0	E_1	Time(s)
bior4.4	1785.516	15.91694	0.943907	7.146816	7.131215	4.2298
sym4	1808.484	15.85781	0.943903	7.146816	7.130978	4.56
db4	1822.385	15.79705	0.94401	7.146816	7.148579	4.4838
sym6	1831.098	15.80091	0.94435	7.146816	7.12959	4.5324
db6	1849.079	15.73329	0.94461	7.146816	7.163433	4.5469
bior6.8	1880.046	15.6889	0.944359	7.146816	7.131286	4.59
coif3	1904.861	15.62146	0.944598	7.146816	7.150794	5.8371
Haar	2163.71	15.08991	0.943961	7.146816	5.840143	4.4867

Based on the results obtained, we conclude that the Haar wavelet performed well when there were small missing regions (Mask 1), achieving the lowest MSE values, indicating an acceptable ability to recover fine details. However, the same wavelet recorded poor results when there were large missing regions. As the MSE value increased, both the PSNR and SSIM decreased significantly compared to the other wavelets. This is attributed to the simplistic nature of the Haar function (its simple structure and very short filter length). It does not have sufficient capacity to represent and analyze complex changes in the image when there are extensive missing regions, which reduces the quality of the visual reconstruction [27][8]. The figure below shows the results obtained for four Haar wavelet masks.

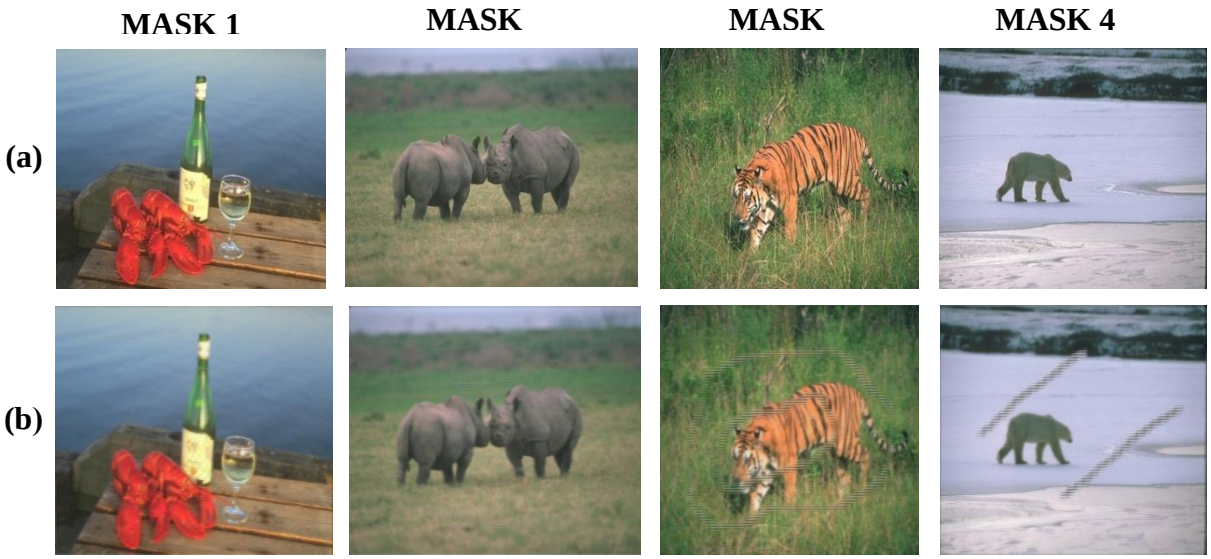

Fig. 4. Examples of inpainting images (a) Original images (b) Inpainted images.

5.2. Different iterations of a numerical solution

In this section, we conducted eight experiments across a variety of wavelets. We studied the behavior of the proposed algorithm for four different mask sizes, each with its own unique size. For each mask, we performed four different iterations, and the experimental results were evaluated using a set of statistical metrics. The goal of the experiment was to determine the relationship between the number of iterations, mask type, and wavelet performance to achieve the best restoration quality and to calculate the execution time to ensure acceptable time efficiency. The iterations chosen for all masks were 1, 5, 9, and 13. Tables 5–12 present the experimental results for eight wavelets.

Table 5. The average values of MSE, PSNR, SSIM, and entropy for image inpainting in Haar (sym1, db1, bior1.1), wavelet at different iterations.

Masks	Iteration	MSE	PSNR	SSIM	E_0	E_1	Time(s)
Mask 1	1	1380.441	17.12084	0.834076	7.146816	5.840143	4.0572
	5	78.98165	30.75424	0.953034	7.146816	5.840143	4.1032
	9	44.2847	35.58406	0.981324	7.146816	5.840143	4.4013
	13	40.15517	36.13894	0.983176	7.146816	5.840143	4.5963
Mask 2	1	2791.834	14.11905	0.823378	7.146816	5.840143	4.0598
	5	460.1534	21.71054	0.876662	7.146816	5.840143	4.1338
	9	156.0644	27.34878	0.930235	7.146816	5.840143	4.4119
	13	98.41994	30.82686	0.961481	7.146816	5.840143	4.696
Mask 3	1	4738.22	11.76953	0.807326	7.146816	5.840143	4.1334
	5	2712	14.09929	0.824988	7.146816	5.840143	4.1755
	9	1673.199	16.08183	0.839124	7.146816	5.840143	4.3431
	13	988.7006	18.33111	0.854798	7.146816	5.840143	4.5152
Mask 4	1	4411.619	12.09584	0.935415	7.146816	5.840143	4.0189
	5	3173.116	13.55673	0.93942	7.146816	5.840143	4.082
	9	2682.841	14.22955	0.941655	7.146816	5.840143	4.2621
	13	2163.71	15.08991	0.943961	7.146816	5.840143	4.4867

Table 6. The average values of MSE, PSNR, SSIM, and entropy for image inpainting in the Sym4 wavelet at different iterations.

Masks	Iteration	MSE	PSNR	SSIM	E_0	E_1	Time(s)
Mask 1	1	1932.863	15.6721	0.827242	7.146816	6.940918	5.1199
	5	101.7422	29.32958	0.93818	7.146816	7.03533	5.503
	9	51.2424	35.09968	0.979375	7.146816	7.079509	5.7371
	13	45.27931	36.90573	0.984495	7.146816	7.104446	5.9405
Mask 2	1	2425.176	14.6606	0.82094	7.146816	7.021724	4.0214
	5	422.2171	22.05141	0.868775	7.146816	7.077201	4.149
	9	142.4681	27.64601	0.918442	7.146816	7.089218	4.3152
	13	84.75701	31.72975	0.956283	7.146816	7.094253	5.0963
Mask 3	1	4180.473	12.28091	0.806406	7.146816	7.140543	4.0682
	5	2340.785	14.72931	0.825952	7.146816	7.161114	4.0932
	9	1460.159	16.66775	0.839385	7.146816	7.174944	4.3778
	13	871.6406	18.87203	0.854087	7.146816	7.160376	4.7001
Mask 4	1	3595.076	12.95333	0.935171	7.146816	6.886795	3.8366
	5	2609.12	14.38109	0.939545	7.146816	7.083904	4.0491
	9	2226.62	15.0254	0.941663	7.146816	7.12288	4.3973
	13	1808.484	15.85781	0.943903	7.146816	7.130978	4.56

Table 7. The average values of MSE, PSNR, SSIM, and entropy for image inpainting in the Sym6 wavelet at different iterations.

Masks	Iteration	MSE	PSNR	SSIM	E_0	E_1	Time(s)
Mask 1	1	1881.401	15.77271	0.82884	7.146816	6.938261	5.0361
	5	108.5202	28.95236	0.935861	7.146816	7.0354	5.9056
	9	53.10803	34.66455	0.977391	7.146816	7.078244	5.4993
	13	45.83697	37.05031	0.984822	7.146816	7.101134	5.7739
Mask 2	1	2353.2	14.77423	0.822606	7.146816	7.02112	4.1886
	5	433.4366	21.9394	0.868289	7.146816	7.079038	4.3065
	9	144.8736	27.60021	0.916468	7.146816	7.089751	4.5181
	13	85.98829	31.61191	0.953837	7.146816	7.094406	4.6976
Mask 3	1	4046.44	12.43008	0.807828	7.146816	7.140235	4.019
	5	2259.335	14.88348	0.827125	7.146816	7.157708	4.181
	9	1414.708	16.80386	0.840318	7.146816	7.173845	4.4377
	13	851.2765	18.97345	0.855084	7.146816	7.159188	4.5665
Mask 4	1	3636.469	12.89604	0.935597	7.146816	6.885841	3.9315
	5	2625.944	14.35069	0.940039	7.146816	7.08274	4.1902
	9	2243.831	14.98808	0.942158	7.146816	7.121301	4.2558
	13	1831.098	15.80091	0.94435	7.146816	7.12959	4.5324

Table 8. The average values of MSE, PSNR, SSIM, and entropy for image inpainting in the db4 wavelet at different iterations.

Masks	Iteration	MSE	PSNR	SSIM	E_0	E_1	Time(s)
Mask 1	1	2410.37	14.83254	0.822684	7.146816	7.057885	3.9734
	5	100.0633	29.4953	0.940495	7.146816	7.042874	4.1882
	9	50.98814	35.25929	0.979886	7.146816	7.079868	4.3877
	13	44.84395	36.95435	0.984812	7.146816	7.103841	4.646
Mask 2	1	3644.701	13.04021	0.814406	7.146816	7.147138	3.9825
	5	415.0179	22.13615	0.869608	7.146816	7.101156	4.1276
	9	140.0055	27.78059	0.920759	7.146816	7.098528	4.3847
	13	84.72335	31.64431	0.956918	7.146816	7.097304	4.6126
Mask 3	1	5387.311	11.24848	0.804142	7.146816	7.225891	4.0538
	5	2507.506	14.40138	0.825886	7.146816	7.229241	4.1302
	9	1458.753	16.66058	0.839851	7.146816	7.214463	4.4926
	13	868.4773	18.88954	0.854272	7.146816	7.186705	4.669
Mask 4	1	4201.821	12.28329	0.933745	7.146816	6.927441	3.9358
	5	2888.341	13.90721	0.93959	7.146816	7.113904	4.1039
	9	2343.106	14.7663	0.941764	7.146816	7.145883	4.3581
	13	1822.385	15.79705	0.94401	7.146816	7.148579	4.4838

Table 9. The average values of MSE, PSNR, SSIM, and entropy for image inpainting in the db6 wavelet at different iterations.

Masks	Iteration	MSE	PSNR	SSIM	E_0	E_1	Time(s)
Mask 1	1	2525.664	14.66109	0.822924	7.146816	7.112008	4.0071
	5	107.2295	29.0681	0.936222	7.146816	7.051293	4.1185
	9	52.53541	35.32754	0.97913	7.146816	7.080478	4.3718
	13	46.06309	37.08348	0.984778	7.146816	7.102581	4.5521
Mask 2	1	3948.215	12.77034	0.81476	7.146816	7.235386	3.97
	5	426.2363	22.02153	0.869329	7.146816	7.120465	4.1703
	9	145.1532	27.60899	0.917831	7.146816	7.107075	4.3372
	13	85.69688	31.72288	0.955588	7.146816	7.099884	4.6615
Mask 3	1	6288.278	10.66517	0.80346	7.146816	7.292701	4.0543
	5	2444.169	14.51184	0.827141	7.146816	7.266331	4.1957
	9	1390.279	16.86836	0.841341	7.146816	7.237555	4.4056
	13	829.1771	19.09319	0.856127	7.146816	7.204098	4.5964
Mask 4	1	5030.85	11.57861	0.933887	7.146816	6.956854	3.9208
	5	3163.434	13.5147	0.939921	7.146816	7.138361	4.1584
	9	2434.531	14.5967	0.942277	7.146816	7.164708	4.4208
	13	1849.079	15.73329	0.94461	7.146816	7.163433	4.5469

Table 10. The average values of MSE, PSNR, SSIM, and entropy for image inpainting in the bior4.4 wavelet at different iterations.

Masks	Iteration	MSE	PSNR	SSIM	E_0	E_1	Time(s)
	1	1907.656	15.7375	0.827579	7.146816	6.94507	5.838
Mask 1	5	103.7953	29.24085	0.936003	7.146816	7.036444	3.967
	9	50.26358	35.41181	0.979932	7.146816	7.07867	4.2111
	13	43.57188	37.45256	0.98569	7.146816	7.101395	4.2156
	1	2418.348	14.6769	0.821203	7.146816	7.027255	4.0448
Mask 2	5	456.5566	21.69951	0.867153	7.146816	7.081213	4.1245
	9	153.6456	27.16633	0.914728	7.146816	7.092596	4.4708
	13	87.39934	31.31131	0.953154	7.146816	7.096048	4.4048
	1	4124.391	12.35236	0.806787	7.146816	7.145774	3.9278
Mask 3	5	2380.551	14.66871	0.825237	7.146816	7.16259	4.1672
	9	1507.401	16.53861	0.837667	7.146816	7.178975	4.2256
	13	912.2014	18.67299	0.851602	7.146816	7.164469	4.4066
	1	3556.076	13.01466	0.935469	7.146816	6.887384	3.8951
Mask 4	5	2578.574	14.4416	0.939649	7.146816	7.084881	4.0062
	9	2195.978	15.08854	0.941718	7.146816	7.122944	4.084
	13	1785.516	15.91694	0.943907	7.146816	7.131215	4.2298

Table 11. The average values of MSE, PSNR, SSIM, and entropy for image inpainting in the bior6.8 wavelet at different iterations.

Masks	Iteration	MSE	PSNR	SSIM	E_0	E_1	Time(s)
	1	1846.839	15.8428	0.831462	7.146816	6.938179	5.1198
Mask 1	5	106.339	29.1914	0.937592	7.146816	7.035228	5.4478
	9	53.30099	35.26744	0.98019	7.146816	7.076496	5.5015
	13	46.51745	37.48613	0.985956	7.146816	7.098623	5.7612
	1	2368.548	14.73576	0.824225	7.146816	7.028563	3.8706
Mask 2	5	457.7584	21.7008	0.86792	7.146816	7.082791	4.0761
	9	156.8968	27.1876	0.914672	7.146816	7.091218	4.435
	13	90.13345	31.5921	0.955376	7.146816	7.093413	4.4584
	1	4083.938	12.37199	0.808785	7.146816	7.155573	3.9348
Mask 3	5	2373.59	14.67015	0.827004	7.146816	7.1664	4.1311
	9	1558.006	16.3946	0.838899	7.146816	7.182894	4.2996
	13	969.2993	18.4142	0.852619	7.146816	7.168238	4.5516
	1	3612.979	12.91975	0.936153	7.146816	6.893806	4.035
Mask 4	5	2628.716	14.33651	0.940369	7.146816	7.086081	4.1693
	9	2265.25	14.94241	0.942357	7.146816	7.123828	4.3689
	13	1880.046	15.6889	0.944359	7.146816	7.131286	4.59

Table 12. The average values of MSE, PSNR, SSIM, and entropy for image inpainting in the Coif3 wavelet at different iterations.

Masks	Iteration	MSE	PSNR	SSIM	E_0	E_1	Time(s)
	1	2424.981	14.8202	0.826198	7.146816	7.071796	6.0397
Mask 1	5	102.4877	29.34631	0.93888	7.146816	7.043731	4.2179
	9	51.29279	35.14836	0.979654	7.146816	7.077895	4.4056
	13	44.74652	37.13688	0.985217	7.146816	7.098869	4.7426
	1	3666.351	13.01579	0.817677	7.146816	7.164895	3.9858
Mask 2	5	446.2219	21.81874	0.869042	7.146816	7.109523	4.4182
	9	150.6017	27.4081	0.916355	7.146816	7.101828	5.6242
	13	87.97494	31.5791	0.955689	7.146816	7.097774	5.9658
	1	5280.489	11.32429	0.806317	7.146816	7.249845	5.382
Mask 3	5	2578.079	14.29383	0.827178	7.146816	7.242238	5.4842
	9	1554.66	16.39788	0.839697	7.146816	7.227635	5.725
	13	949.2711	18.50603	0.853067	7.146816	7.198578	5.959
	1	4207.998	12.2679	0.93469	7.146816	6.939096	5.1952
Mask 4	5	2908.158	13.88423	0.94052	7.146816	7.117298	5.2432
	9	2398.621	14.67831	0.942583	7.146816	7.148748	5.5373
	13	1904.861	15.62146	0.944598	7.146816	7.150794	5.8371

The results of the above experiments showed the following:

1. The performance of wavelets varies depending on the size and shape of the lost region. The optimal choice remains dependent on the type of loss: Haar for small loss, db4 for medium loss, and bior4.4 and bior6.8 for large loss, when preserving the optical structure (SSIM) is paramount. It can be argued that db6 is the most stable and efficient, especially in complex cases, due to its high number of vanishing moments and its superior ability to reconstruct fine details [28]. Meanwhile, bior4.4 combined high quality with a shorter execution time due to its shorter filters. These results reflect that the choice of wavelet is directly related to its mathematical properties (symmetry, linear phase, filter length, vanishing moments) and the nature of the gaps (small/large) [29][30].

2. The results also showed that the best restoration quality was achieved with approximately 13 iterations. The scientific reason is that the wavelet transforms aggregate image energy into a few high-value coefficients, making it easier for the Cahn-Hilliard model to quickly propagate general structures in the initial phase. After this point, increasing iterations leads to over-smoothing and loss of fine details [3] [31].

3. The hybrid modelling of the Cahn-Hilliard and wavelet transform has proven highly effective in image restoration within missing regions of varying sizes. It provides a propagation environment that preserves structure across gaps and allows for high quality after a few iterations, due to the stability of the numerical scheme and the speed of computation in the wavelet domain [32][33]. Long wavelets with high vanishing moments also contributed to reducing MSE and increasing PSNR, while symmetric biphasic wavelets (Sym, Bior) preserved spatial structure and increased SSIM [33][34]. Figure 5 below illustrates the visual study of the outcomes in the db6 wavelet for the restoration of mask 3 across four iterations.

(e) **(f)**

Fig. 5. Examples of inpainting images. (a) Original image. (b) Mask image. (c), (d), (e), and (f) Inpainted images in db6 Wavelet at iterations (1, 5, 9, and 13, respectively).

6. Conclusion and future work

The hybrid approach based on the Cahn-Hilliard diffusion model and wavelet transform provides an effective framework for restoring images with missing regions. The results indicate that the gap's nature directly influences the choice of wavelet. Haar demonstrated excellent performance with small gaps, while db6 and bior4.4 achieved the best performance with large gaps in terms of reducing MSE and increasing PSNR in a shorter time. The success is attributed to the combination of the mathematical properties of the wavelet and the diffusion model's ability to preserve the visual structure of the image. This combination provides numerical stability, allowing for high quality after a limited number of iterations. From a future perspective, this hybrid approach could be enhanced by developing parallel algorithms using GPUs to reduce execution time, paving the way for its application in practical.

Conflict of Interest Statement: No potential conflicts of interest were reported by the authors or editors involved in this work.

References

[1] Z. A. A. Kareem and A. K. Al-Jaberi, "A Novel Image Inpainting Technique Based on Isotropic Diffusion," *Basrah J. Sci.*, vol. 40, no. 2, pp. 289–305, 2022. DOI: 10.29072/basjs.20220203

[2] A. K. Al-Jaberi, A. Asaad, S. A. Jassim, and N. Al-Jawad, "Topological data analysis to improve exemplar-based inpainting," in *Mobile Multimedia/Image Processing, Security, and Applications 2018*, SPIE, 2018, pp. 13–24. DOI: 10.1117/12.2309931

[3] Y. Huang *et al.*, "Wavedm: Wavelet-based diffusion models for image restoration," *IEEE Trans. Multimed.*, vol. 26, pp. 7058–7073, 2024. DOI: 10.1109/TMM.2024.3359769

[4] Z. A. A. Kareem and A. K. Al-Jaberi, "Removing Text and Inpainting Irregular Regions in Digital Images within Spatial and Frequency Domains," *Basrah J. Sci.*, vol. 43, no. 1, pp. 35–50, 2025. DOI: 10.29072/basjs.20250103

[5] A. Kiruluta and A. Lemos, "A hybrid wavelet-fourier method for next-generation conditional diffusion models," *arXiv Prepr. arXiv2504.03821*, 2025. DOI: 10.48550/arXiv.2504.03821

[6] Y. Yu *et al.*, "Wavefill: A wavelet-based generation network for image inpainting," in *Proceedings of the IEEE/CVF international conference on computer vision*, 2021, pp. 14114–14123. DOI: 10.1109/ICCV48922.2021.01385

[7] R. H. Chan, S. Setzer, and G. Steidl, "Inpainting by flexible Haar-wavelet shrinkage," *SIAM J.*

Imaging Sci., vol. 1, no. 3, pp. 273–293, 2008. DOI:https://doi.org/10.1137/070711499
[8] T. F. Chan, J. Shen, and H.-M. Zhou, "Total variation wavelet inpainting," *J. Math. Imaging Vis.*, vol. 25, no. 1, pp. 107–125, 2006) . DOI: 10.1007/s10851-006-5257-3
[9] A. Averbuch, P. Neittaanmäki, V. Zheludev, M. Salhov, and J. Hauser, "Image inpainting using directional wavelet packets originating from polynomial splines," *Signal Process. Image Commun.*, vol. 97, p. 116334, 2021) .DOI : 10.1007/s10444-023-10024-4
[10] S. He, G. Lin, T. Li, and Y. Chen, "Frequency-Domain Fusion Transformer for Image Inpainting," *arXiv Prepr. arXiv2506.18437*, 2025. DOI: https://doi.org/10.48550/arXiv.2506.18437
[11] B. Dong, Q. Jiang, and Z. Shen, "Image restoration: Wavelet frame shrinkage, nonlinear evolution pdes, and beyond," *Multiscale Model. Simul.*, vol. 15, no. 1, pp. 606–660, 2017.DOI: https://doi.org/10.1137/15M1037457
[12] H. Zhang and S. Dai, "Image inpainting based on wavelet decomposition," *Procedia Eng.*, vol. 29, pp. 3674–3678, 2012) .DOI: 10.1016/j.proeng.2012.01.551
[13] R. H. Chan, J. Yang, and X. Yuan, "Alternating direction method for image inpainting in wavelet domains," *SIAM J. Imaging Sci.*, vol. 4, no. 3, pp. 807–826, 2011. DOI: https://doi.org/10.1137/100807247
[14] W. Guo and L.-H. Qiao, "Inpainting based on total variation," in *2007 International Conference on Wavelet Analysis and Pattern Recognition*, IEEE, 2007, pp. 939–943. DOI: https://doi.org/10.1109/ICWAPR.2007.4420804
[15] Y. Cao, R. Ma, K. Zhao, and P. An, "WFIL-NET: image inpainting based on wavelet downsampling and frequency integrated learning module," *Multimed. Syst.*, vol. 31, no. 1, p. 21, 2025. DOI: https://doi.org/10.1007/s00530-024-01609-0
[16] D. O. Kolodochka and M. V Polyakova, "LAMA-WAVELET: IMAGE IMPAINTING WITH HIGH QUALITY OF FINE DETAILS AND OBJECT EDGES," *Radio Electron. Comput. Sci. Control*, no. 1, p. 208, 2024.DOI: https://doi.org/10.15588/1607-3274-2024-1-19
[17] A. L. Bertozzi, S. Esedoglu, and A. Gillette, "Inpainting of binary images using the Cahn–Hilliard equation," *IEEE Trans. image Process.*, vol. 16, no. 1, pp. 285–291, 2006. DOI: https://doi.org/10.1109/TIP.2006.887728
[18] J. W. Cahn and J. E. Hilliard, "Free energy of a nonuniform system. I. Interfacial free energy," *J. Chem. Phys.*, vol. 28, no. 2, pp. 258–267, 1958. DOI: https://doi.org/10.1109/TIP.2006.887728
[19] Y. Zhang, H. Zheng, X. Xu, and H. Zhu, "HVI-Based Spatial–Frequency-Domain Multi-Scale Fusion for Low-Light Image Enhancement.," *Appl. Sci.*, vol. 15, no. 19, 2025. DOI: https://doi.org/10.3390/app151910376
[20] X. Guan, R. He, L. Wang, H. Zhou, Y. Liu, and H. Xiong, "DWTMA-Net: Discrete Wavelet Transform and Multi-Dimensional Attention Network for Remote Sensing Image Dehazing," *Remote Sens.*, vol. 17, no. 12, p. 2033, 2025. DOI: https://doi.org/10.3390/rs17122033
[21] K. E. C. Vidyasagar, K. R. Kumar, G. N. K. A. Sai, M. Ruchita, and M. J. Saikia, "Signal to image conversion and convolutional neural networks for physiological signal processing: A review," *Ieee Access*, vol. 12, pp. 66726–66764, 2024. DOI: https://doi.org/10.1109/ACCESS.2024.3399114
[22] A. K. Al-Jaberi, S. A. Jassim, and N. Al-Jawad, "Colourizing monochrome images," in *Mobile Multimedia/Image Processing, Security, and Applications 2018*, SPIE, 2018, pp. 25–37. DOI: https://doi.org/10.3390/rs17122033
[23] K. Gu, S. Wang, G. Zhai, W. Lin, X. Yang, and W. Zhang, "Analysis of distortion distribution for pooling in image quality prediction," *IEEE Trans. Broadcast.*, vol. 62, no. 2, pp. 446–456, 2016. DOI: https://doi.org/10.1109/TBC.2015.2511624
[24] A. C. Bovik, *Handbook of image and video processing*. Academic press, 2010. DOI: https://doi.org/10.1016/B978-0-12-119792-6.x5062-1
[25] Z. Wang, A. C. Bovik, H. R. Sheikh, and E. P. Simoncelli, "Image quality assessment: from error visibility to structural similarity," *IEEE Trans. image Process.*, vol. 13, no. 4, pp. 600–612, 2004. DOI: https://doi.org/10.1109/TIP.2003.819861
[26] A. Singhal, R. P. Singh, and M. Tenguria, "Comparison of different wavelets for watermarking

of colored images," in *2011 3rd International Conference on Electronics Computer Technology*, IEEE, 2011, pp. 187–191. DOI: https://doi.org/10.1109/ICECTECH.2011.187

[27] H. Wu, F. He, Y. Duan, X. Yan, and B. Fan, "Haar-wavelet based texture inpainting for human pose transfer," *Inf. Process. Manag.*, vol. 61, no. 3, p. 103612, 2024. DOI: https://doi.org/10.1016/j.ipm.2023.103612

[28] P. Viswanathan and K. Palanisamy, "An Empirical Selection of Wavelet for Near-lossless Medical Image Compression," 2024. DOI: https://doi.org/10.2174/1573405620666230330113833

[29] H. Li and K. Xu, "Innovative adaptive edge detection for noisy images using wavelet and Gaussian method," *Sci. Rep.*, vol. 15, no. 1, p. 5838, 2025. DOI: https://doi.org/10.1038/s41598-025-86860-9

[30] W. Wronka, "Optimal mother wavelet selection for a stochastic resynthesis of the sound textures," *Vib. Phys. Syst.*, vol. 34, no. 2, 2023. DOI: https://vibsys.put.poznan.pl/article/optimal-mother-wavelet-selection-for-a-stochastic-resynthesis-of-the-sound-textures/

[31] T. Xu *et al.*, "Uncovering the over-smoothing challenge in image super-resolution: Entropy-based quantification and contrastive optimization," *IEEE Trans. Pattern Anal. Mach. Intell.*, vol. 46, no. 9, pp. 6199–6215, 2024. DOI: https://doi.org/10.1109/TPAMI.2024.3378704

[32] Y. Awad, H. Fakih, and Y. Alkhezi, "Numerical Linear Algebra for the Two-Dimensional Bertozzi–Esedoglu–Gillette–Cahn–Hilliard Equation in Image Inpainting," *Mathematics*, vol. 11, no. 24, p. 4952, 2023. DOI: https://doi.org/10.3390/math11244952

[33] I. H. Latif, S. H. Abdulredha, and S. K. A. Hassan, "Discrete wavelet transform-based image processing: A review," *Al-Nahrain J. Sci.*, vol. 27, no. 3, pp. 109–125, 2024. DOI: https://doi.org/10.22401/ANJS.27.3.13

[34] Y. Guo *et al.*, "A Novel and Optimized Sine–Cosine Transform Wavelet Threshold Denoising Method Based on the Sym4 Basis Function and Adaptive Threshold Related to Noise Intensity," *Appl. Sci.*, vol. 13, no. 19, p. 10789, 2023. DOI: https://doi.org/10.3390/app131910789

Journal of Basrah Researches (Sciences) **51**(2), 116 (2025)
DOI: https://doi.org/10.56714/bjrs.51.2.9

تلوين الصور الهجينة باستخدام نموذج Chan-Hillard وWavelet

ندى سرحان. الفرطوسي*، أحمد كاظم الجابري

قسم الرياضيات، كلية التربية للعلوم الصرفة، جامعة البصرة، العراق.

معلومات البحث

الاستلام 27 أيلول 2025
المراجعة 25 تشرين اول 2025
القبول 30 تشرين اول 2025
النشر 31 كانون اول 2025

الكلمات المفتاحية

تلوين الصورة، المجال الترددي، تحويل الموجة المنفصلة (DWT)، معادلة كاهن-هيليارد، طريقة الفروق المحدودة الضمنية.

الملخص

مع مجموعة واسعة من التطبيقات في معالجة الصور الرقمية، بما في ذلك تحرير الوسائط المتعددة، والتصوير الطبي، وحفظ التراث الثقافي، تُعدّ استعادة الصور مهمةً أساسية. في هذا العمل، نُقدّم إطار عمل هجينًا لاستعادة الصور يجمع بين نموذج انتشار قائم على معادلة كاهن-هيليارد وتحويل مويجات أحادي المستوى لتحليل الصورة إلى مكونات ترددية مميزة. وللحفاظ على استمرارية البنية، تُوظّف هذه الطريقة الهجينة فوائد المويجات في مجال التردد لإعادة بناء النسيج وقدرات انتشارها في المجال المكاني. لتحقيق انتشار سلس للمعلومات والحفاظ على حدة الحواف، يُستخدم نهج الفرق المحدود الضمني لحل المشكلة عدديًا. حُلّلت تأثيرات عدة أنواع من الموجات، بما في ذلك Haar وdb1 وsym1 وbior1.1 وdb4 وsym4 وcoif3 وغيرها. تُشير النتائج إلى أن أداء المويجات يختلف باختلاف طول الدعامة وسلاسة الدوال الأساسية، وتُقدّم إرشادات عملية لاختيار المويجة الأنسب لاستعادة الصور في تطبيقات معالجة الصور الحديثة.

Citation: N. S. AL-Fartosi, A. K. Al-Jaberi, J. Basrah Res. (Sci.) **50**(2), 116 (2025). DOI:https://doi.org/10.56714/bjrs.51.2.9

***Corresponding author email:** nada.sarhan@uobasrah.edu.iq

ISSN: 1817-2695 (Print); 2411-524X (Online)
Online at: https://jou.jobrs.edu.iq